Instability modes of a two-layer Newtonian plane Couette flow past a porous medium

A. Ananth Praveen Kumar,[1] Himanshu Goyal,[1] Tamal Banerjee,[1] and Dipankar Bandyopadhyay[1,2,*]
[1]*Department of Chemical Engineering, Indian Institute of Technology, Guwahati, India*
[2]*Centre for Nanotechnology, Indian Institute of Technology, Guwahati, India*
(Received 30 January 2013; published 5 June 2013)

We explore the salient features of the different instability modes of a pressure-driven two-layer plane Couette flow confined between a moving wall and a Darcy-Brinkman porous layer. A linear stability analysis of the conservation laws leads to an Orr-Sommerfeld system, which is solved numerically with appropriate boundary conditions to identify the time and length scales of the instability modes. The study reveals that the movement of the confining wall together with the slippage at the porous-liquid interface originating from the flow inside the porous layer can stimulate a pair of finite-wave-number shear modes in addition to the long-wave interfacial mode of instability. The shear modes dominate the interfacial mode, especially when the frictional influence at the liquid layers is smaller due to the movement of the confining plate or due to the larger slippage at the porous-liquid interface. The shear modes are found to be present under all combinations of the viscosity μ_r and thickness h_r ratios of the liquid layers. This is in stark contrast to the two-layer flow confined between nonporous plates where the interfacial (shear) mode is observed only when $\mu_r > h_r^2$ ($\mu_r < h_r^2$). Interestingly, the strength of one of the shear modes is found to increase with the velocity of the bounding moving plate, whereas the other shear mode gains strength in the presence of highly porous, permeable, and thick porous layers. The results reported can be of significant importance in the microscale two-phase flows where the presence of a bounding porous layer or moving wall can expedite the intermixing of layers to improve the multiphase mixing, heat and mass transfer, and emulsification characteristics.

DOI: 10.1103/PhysRevE.87.063003 PACS number(s): 47.56.+r, 68.15.+e, 47.20.Ft, 47.61.Jd

I. INTRODUCTION

The stability and dynamics of the pressure-driven stratified flow of a pair of liquid layers have been studied comprehensively over the years because of their presence in a variety of important scientific and technological prototypes such as oil-water flow, extrusion of polymers [1–3], electrochemical cells [4], fuel cells [5], microfluidic devices [6,7], and bioprocesses [8]. Previous theoretical [9–27] and experimental [28,29] studies suggest that the two-layer pressure-driven Poiseuille flow (PPF) or Couette flow (CF) can become unstable either through the long-wave interfacial mode or the finite-wave-number shear mode. Yih [9] was the first to observe that the viscosity stratification across the interface of a two-layer PPF develops an interfacial mode in the friction-dominated low-speed flows [9]. Subsequent studies showed that the two-layer flows can also develop a Tollmein-Schlichting-type finite-wave-number shear mode beyond a threshold flow rate where the inertial force dominates the frictional force [11]. Importantly, a pair of equal density immiscible liquids undergoing PPF is found to be neutrally stable when $\mu_r = h_r^2$, while it develops the interfacial mode (shear mode) of instability for the condition $\mu_r > h_r^2$ ($\mu_r < h_r^2$) [15,20]. Here the notations μ_r and h_r denote viscosity and the thickness ratios of the liquid layers, respectively. A number of reviews [30–33] ably summarize the other salient features of the macroscopic two-layer stratified flows.

Studies related to the instabilities of multiphase fluid flows in microscale devices have regained impetus in the recent times owing to their significance in mixing, separation, heat and mass transfer, and pumping applications [34–45]. Flow dynamics in microscale devices are found to be notably different from similar macroscopic configurations because of (i) the strong frictional influence arising from the surrounding confinements, (ii) the prominence of the capillary and adhesive forces in the flow dynamics, and (iii) even a trifling amount of roughness, porosity, or slippage at the boundaries, which can profoundly alter the flow patterns. Clearly, the presence of air pockets, physicochemical defects, or pores at the bounding walls can easily invoke hydrodynamic instabilities to the fluid lamellae, which can further be exploited in improving the mixing and heat and mass transfer efficiencies. A number of previous studies indicate that even at the macroscopic level, the presence of a porous layer can influence the flow patterns.

Beavers and Joseph [46] showed that the salient features of the instabilities of the flow of a liquid layer on a porous bed can be explored by simply enforcing a simple slip boundary condition at the porous-liquid interface. Later it was found that the Darcy law together with the equations of motion for the fluid can more comprehensively reveal the influence of the properties of the porous medium on the free-surface instabilities of a film flowing down an inclined porous plane [47–50]. Recent studies employ a more generic Darcy-Brinkman approach for the porous medium [51] and reveal the influence of the porosity, permeability, and stress-jump coefficient on the free-surface instabilities of a thin film flowing over porous substrates [52–62]. Importantly, the studies show that the presence of a porous layer underneath a single liquid layer can induce a finite-wave-number shear mode, which gains strength with an increase in the porosity, permeability, and thickness of the porous layer. The studies also highlight the conditional presence of multiple shear modes

*Author to whom correspondence should be addressed: dipban@iitg.ernet.in

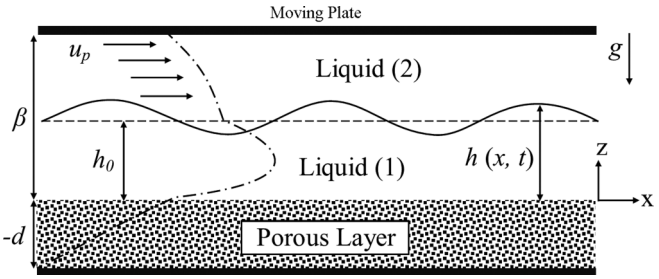

FIG. 1. Schematic diagram of a two-layer flow inside a channel confined between a porous layer at the bottom and a moving substrate at the top.

in which one of the shear modes appears because of the presence of the porous medium [60–62]. In this context, the hydrodynamic stability of a two-layer CF on a porous layer (Fig. 1) is another exciting configuration.

In the present work, the instability of a planar two-layer Couette flow confined between a rigid and a Darcy-Brinkman porous medium (CFPM) is investigated through a detailed Orr-Sommerfeld (OS) analysis. The study seamlessly compares and contrasts both macro- and microscopic features of the different instability modes of the CFPM. Similar to two-layer PPF, the CFPM is found to be unstable through the long-wave interfacial and the finite-wave-number shear modes. Interestingly, we observe the presence of twin shear modes for a CFPM in which one shows its dependence on the velocity of the bounding surface, whereas the other is responsive to the flow inside the porous layer. The strengths of these shear modes are tunable with the thickness, porosity, and permeability of the porous layer together with the plate velocity, whereas the interfacial mode remains rather insensitive to these changes. The shear modes emerge stronger than the interfacial mode when the frictional influence is reduced in the CFPM by increasing the porosity, thickness, and permeability of the porous layer or when the bounding plate velocity is faster. The conditions for the coexistence and dominance of all these modes are explored for a large parameter space, which can be of importance in the studies related to the microscale mixing and heat and mass transfer employing two-layer flows.

The paper is organized in the following manner. In Sec. II, the details of the governing equations and boundary conditions are shown. Brief outlines of the base-state equations and the analysis on the base-state velocity profiles are presented in Sec. III. In Sec. IV, brief outlines of the linear stability analysis are presented. In Sec. V, the numerical methods to solve the OS system are discussed and the results are validated against previous investigations. The other results are analyzed in Sec. VI before summarizing in Sec. VII.

II. PROBLEM FORMULATION

Figure 1 schematically shows a typical pressure-driven two-layer CFPM. The liquid films are assumed to be of Newtonian, immiscible, incompressible (constant density ρ_j), and constant viscosity μ_j. The subscripts 1, 2, and m of the variables represent the upper, lower, and porous layers, respectively. A two-dimensional Cartesian coordinate system is employed for the formulation along the x and z directions. The continuity and the equations of motion for the fluid layers ($j = 1$ and 2) are

$$\nabla \cdot \mathbf{u}_j = 0, \tag{1}$$

$$\rho_j[\dot{\mathbf{u}}_j + (\mathbf{u}_j \cdot \nabla)\mathbf{u}_j] = -\nabla p_j + \mu_j \nabla^2 \mathbf{u}_j + \rho_j \mathbf{g}. \tag{2}$$

Here $\mathbf{g}$, $\mathbf{u}_j\{u_j, w_j\}$, and p_j represent acceleration due to gravity, velocity vector, and pressure for the jth layer, respectively. The overdots represent the time derivative. The continuity and the equations of motion for the Darcy-Brinkman porous medium [51–62] are

$$\nabla \cdot \mathbf{u}_m = 0, \tag{3}$$

$$\frac{\rho_1}{b}\dot{\mathbf{u}}_m = -\nabla p_m + \mu_e \nabla^2 \mathbf{u}_m - \frac{\mu_1}{\kappa}\mathbf{u}_m + \rho_1 \mathbf{g}. \tag{4}$$

The porous medium has the effective viscosity μ_e, porosity $b = \mu_1/\mu_e$, permeability κ, and thickness d. At the porous solid ($z = -d$), no-slip and impermeability boundary conditions ($\mathbf{u}_m = 0$) are enforced. The impermeable upper plate ($w_2 = 0$) moves with a finite velocity ($u_2 = u_p$) at the liquid-solid interface ($z = \beta$). The continuity of velocities ($\mathbf{u}_1 = \mathbf{u}_m$), normal stresses balance ($-p_m + 2\mu_e w_{m_z} = -p_1 + 2\mu_1 w_{1_z}$), and tangential stress jump ($\mu_e u_{m_z} - \mu_1 u_{1_z} = \xi u_m/\sqrt{\kappa}$) are enforced as boundary conditions at the rigid-lower-layer–porous-medium interface ($z = 0$). Here the symbol ξ is the stress-jump coefficient [51,52]. The tangential ($\mathbf{t} \cdot \bar{\boldsymbol{\tau}}_2 \cdot \mathbf{n} = \mathbf{t} \cdot \bar{\boldsymbol{\tau}}_1 \cdot \mathbf{n}$) and normal ($\mathbf{n} \cdot \bar{\boldsymbol{\tau}}_2 \cdot \mathbf{n} - \mathbf{n} \cdot \bar{\boldsymbol{\tau}}_1 \cdot \mathbf{n} = \gamma\, \nabla \cdot \mathbf{n}$) stress balances, the continuity of the velocities $\mathbf{u}_1 = \mathbf{u}_2$, and the kinematic condition $\dot{h} = -u_1(\partial h/\partial x) + w_1$ are enforced as boundary conditions at the deformable liquid-liquid interface ($z = h$). Here γ represents the interfacial tension of the liquid-liquid interface and $\bar{\boldsymbol{\tau}}_j = \mu_j(\nabla \mathbf{u_j} + \nabla \mathbf{u}_j^T)$ is the Newtonian stress tensor. The symbols $\mathbf{n}$ and $\mathbf{t}$ represent the outward normal vector $(-h_x/\sqrt{1+h_x^2}, 1/\sqrt{1+h_x^2})$ and the corresponding tangent vector $(1/\sqrt{1+h_x^2},\ h_x/\sqrt{1+h_x^2})$, respectively. The subscripts x and z denote the partial derivatives of the respective variables.

The governing equations (1)–(4) and the boundary conditions are transformed into nondimensional forms employing the thickness of the lower layer h_0 as the length scale and the viscous time scale $\rho_1 h_0^2/\mu_1$. The other dimensionless variables employed for this purpose are $X = x/h_0$, $Z = z/h_0$, $H = h/h_0$, $T = t\mu_1/\rho_1 h_0^2$, $\mathbf{U}_j = \mathbf{u}_j \rho_1 h_0/\mu_1$, $V = u_p h_0 \rho_1/\mu_1$, $\rho_r = \rho_2/\rho_1$, $\mu_r = \mu_2/\mu_1$, $B = \beta/h_0$, $h_r = B - 1$, $D_m = d/h_0$, $G = g h_0^3 \rho_1^2/\mu_1^2$, and $P_j = p_j h_0^2 \rho_1/\mu_1^2$. The resulting dimensionless continuity equations for the liquid layers ($i = 1$ and 2) and the porous medium ($i = m$) are

$$\nabla \cdot \mathbf{U}_i = 0. \tag{5}$$

The dimensionless equations of motions for the liquid layers and the porous layer are

$$\dot{\mathbf{U}}_1 + \mathbf{U}_1 \cdot \nabla \mathbf{U}_1 = -\nabla P_1 + \nabla^2 \mathbf{U}_1 + \mathbf{G}, \tag{6}$$

$$\rho_r(\dot{\mathbf{U}}_2 + \mathbf{U}_2 \cdot \nabla \mathbf{U}_2) = -\nabla P_2 + \mu_r \nabla^2 \mathbf{U}_2 + \rho_r \mathbf{G}, \tag{7}$$

$$(1/b)\dot{\mathbf{U}}_m = -\nabla P_m + (1/b)\nabla^2 \mathbf{U_m} - (1/\mathrm{Da})\mathbf{U_m} + \mathbf{G}. \tag{8}$$

The unperturbed lower, upper, and porous layers occupy the domains $0 \leqslant Z \leqslant H$, $H \leqslant Z \leqslant B$, and $-D_m \leqslant Z \leqslant 0$, respectively. The dimensionless no-slip and impermeability boundary conditions ($\mathbf{U}_m = 0$) are enforced at the porous-solid interface ($Z = -D_m$). The impermeable plate ($W_2 = 0$) at the upper liquid-solid interface ($Z = B$) moves with a uniform dimensionless velocity $U_2 = V$. The continuity of velocities ($\mathbf{U}_1 = \mathbf{U}_m$), normal stress balance $[P_1 - P_m + 2(W_{mZ}/b - W_{1Z}) = 0]$, and stress jump $[U_{mZ}/b - U_{1Z} - (\chi/\sqrt{\mathrm{Da}})U_m = 0]$ are enforced at the liquid-porous interface ($Z = 0$). The continuity of velocities $\mathbf{U}_1 = \mathbf{U}_2$, the kinematic equation $\dot{H} = -U_1 H_X + W_1$, the normal

$$P_2 - P_1 + \frac{2}{\left[1 + H_X^2\right]}\left\{\left[\left(1 - H_X^2\right)W_{1Z} - H_X(W_{1X} + U_{1Z})\right] - \mu_r\left[\left(1 - H_X^2\right)W_{2Z} - H_X(W_{2X} + U_{2Z})\right]\right\} = \frac{\Gamma H_{XX}}{\left[1 + H_X^2\right]^{3/2}},$$

and the shear

$$\left[(U_{1Z} + W_{1X})\left(1 - H_X^2\right) + 2H_X(W_{1Z} - U_{1X})\right] = \mu_r\left[(U_{2Z} + W_{2X})\left(1 - H_X^2\right) + 2H_X(W_{2Z} - U_{2X})\right]$$

stress balances are enforced at the liquid-liquid interface $Z = H$. The subscripts X and Z in the expressions denote partial derivatives. In what follows, the formulations and discussion are carried out in terms of nondimensional variables such as the Darcy number $\mathrm{Da} = \kappa/h_0^2$, which represents permeability; $\chi = \xi/\mu_1$, which represents the stress-jump coefficient; $b = \mu_1/\mu_e$, which represents porosity; $D_m = d/h_0$, which represents the thickness of the porous layer; G, the Galileo number; and $\Gamma = \gamma h_0/\rho_1 \nu_1^2$, the capillary number.

III. BASE-STATE ANALYSIS

The governing equations are solved for the unperturbed interface [$H = 1$, $\bar{W}_j = 0$, and $U_j = \bar{U}_j(Z)$ ($j = 1$, 2, and m)] and the following base-state solutions of the x-directional flow are obtained:

$$\bar{U}_1 = C_{11}Z^2 + C_{12}Z + C_{13}, \quad 0 \leqslant Z \leqslant 1, \tag{9}$$

$$\bar{U}_2 = C_{21}Z^2 + C_{22}Z + C_{23}, \quad 1 \leqslant Z \leqslant B, \tag{10}$$

$$\bar{U}_m = C_{m1}e^{MZ} + C_{m2}e^{-MZ} + C_{m3}, \quad -D_m \leqslant Z \leqslant 0. \tag{11}$$

The global constraint that the volumetric flow rate $Q = \int_{-D_m}^{0} \bar{U}_m + \int_0^1 \bar{U}_1 + \int_1^B \bar{U}_2$ in the channels is correlated to the base-state pressure gradient by the cumbersome relation

$$P_{0X} = \frac{\begin{array}{l} 6G^*\{-4\mathrm{Da}(F_+ - 1)^2F_-\mu_r + M[(B-1)^2 - \mu_r]a_2\}a_3 + 6M\mu_r a_1^2(2V\mu_r + G^*\rho_r a_5) \\ + 3G^*\{-2(F_+ - 1)^2F_-\mu_r + M[(B-1)^2 - \mu_r]\phi\}a_4 \\ + a_1(2M\{-6(Q + V - BV)\mu_r + G^*[3 - 6B + 3B^2 - \mu_r + 6D\mathrm{Da}\mu_r + 2(B-1)^3\rho_r]\}a_3 \\ - 6G^*M\mu_r a_4 + 3\{2(F_+ - 1)^2F_-\mu_r + M[-(B-1)^2 + \mu_r]\phi\}(2V\mu_r + G^*\rho_r a_5)) \end{array}}{\begin{array}{l} (-2\{12\mathrm{Da}(F_+ - 1)^2F_-\mu_r + M[-1 + (3 - 2B)B^2 + \mu_r - 6D\mathrm{Da}\mu_r]a_1 + 3M[-(B-1)^2 + \mu_r]a_2\} \\ a_3 + 3\{2(F_+ - 1)^2F_-\mu_r + M[-(B-1)^2 + \mu_r]\phi + 2M\mu_r a_1\}(a_1a_5 - a_4)) \end{array}}. \tag{12}$$

Here the velocities with overbars $\bar{U}_1$, $\bar{U}_2$, and $\bar{U}_m$ represent the base-state solutions at the lower, upper, and porous layers, respectively. The constants C_{ij} ($i = 1$, 2, and m; $j = 1$, 2, and 3) in expressions (9)–(11) are determined from the base-state governing equations and boundary conditions as presented in the Appendix and $M = \sqrt{b/\mathrm{Da}}$.

Figure 2 shows the nondimensional base-state velocity profiles for a CFPM under varied conditions. Figure 2(a) shows the influence of the velocity of the confining plate at the top V of the flow profiles. The curves clearly indicate that the CFPM is under the coupled influence of the slippage at the porous-liquid interface originating from the flow inside the underlying porous layer together with the motion of the confining plate. The location of the maximum velocity in the profile is observed in the lower layer because the viscosity of the upper layer is considered higher (solid line). The dashed lines suggest that with an increase in the plate velocity the relative strength of the inertial force become stronger than the viscous resistance. In such situations, the flow rate at the highly viscous upper layer becomes faster and the location of the maximum velocity at the lower layer progressively moves towards the upper layer. Figures 2(b)–2(d) together show that when V is kept constant, an increase in the porosity b, permeability Da, and thickness of the porous layer D_m can cause a stronger flow inside the porous layer, which in turn can impart a stronger slippage at the porous-liquid interface. Thus, for a confined CFPM, a moving boundary and the presence of a bounding porous surface can lead to a stronger flow inside the channel, which in turn can induce instabilities by suppressing the frictional resistance.

IV. LINEAR STABILITY ANALYSIS

The nondimensional governing equations and the boundary conditions are linearized by imposing small-amplitude perturbations to the base state: $U_j = \bar{U}_j + U_j'$, $W_j = W_j'$, and $P_j = \overline{P}_j + P_j'$, where $j = 1$, 2, and m. The overbars indicate the base state and the primes denote perturbed quantities. The equations for velocity perturbations are then transformed in terms of the stream functions as $U_j' = \partial\Psi_j/\partial Z$ and

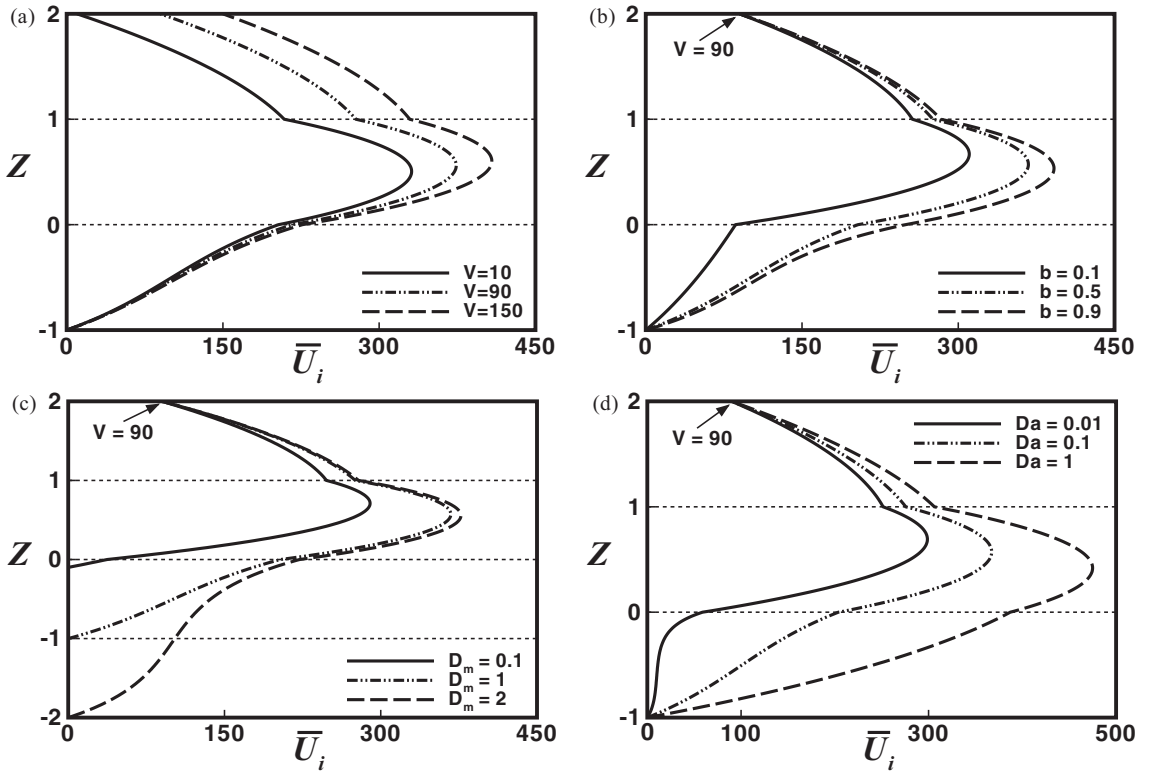

FIG. 2. Plots showing the nondimensional base-state velocity $\bar{U}_i$ profiles across the width of the channel Z for $\mu_r = 5$, $\rho_r = 1$, $h_r = 1$, $b = 0.5$, $\chi = 0.1$, $\mathrm{Da} = 0.1$, and $D_m = 1$.

$W_j' = -\partial\Psi_j/\partial X$. The resulting governing equations and the boundary conditions are linearized by employing the normal linear modes $\Psi_j(X,Z,T) = \tilde{\Psi}_j(Z)\,e^{\mathbf{i}K(X-CT)}$, $P_j'(X,Z,T) = \tilde{P}_j(Z)\,e^{\mathbf{i}K(X-CT)}$, and $H(X,Z,T) = 1 + \tilde{H}e^{\mathbf{i}K(X-CT)}$ to obtain the following dimensionless coupled OS equations for the liquid layers and the porous medium:

$$(D^2 - K^2)^2\tilde{\Psi}_1 = \mathbf{i}K[(\bar{U}_1 - C)(D^2 - K^2) - D^2\bar{U}_1]\tilde{\Psi}_1, \quad (13)$$

$$\nu_r(D^2 - K^2)^2\tilde{\Psi}_2 = \mathbf{i}K[(\bar{U}_2 - C)(D^2 - K^2) - D^2\bar{U}_2]\tilde{\Psi}_2, \quad (14)$$

$$(D^2 - K^2)^2\tilde{\Psi}_m = (b/\mathrm{Da} - \mathbf{i}KC)(D^2 - K^2)\tilde{\Psi}_m. \quad (15)$$

The notation D represent the differentiation d/dZ, ν_r $(=\mu_r/\rho_r)$, K is the wave number, and C $(=C_r + \mathbf{i}C_i)$ is the phase speed, with C_r and KC_i the wave speed and the growth rate of the perturbation, respectively. Here C_r and C_i are the real and imaginary parts of the wave speed, respectively. The linearized nondimensional boundary conditions at the porous-solid and liquid-solid boundaries are

$$\tilde{\Psi}_{mZ}(-D_m) = \tilde{\Psi}_m(-D_m) = \tilde{\Psi}_{2Z}(B) = 0, \quad \tilde{\Psi}_2(B) = V. \quad (16)$$

At the porous-liquid interface ($Z = 0$),

$$\tilde{\Psi}_1 = \tilde{\Psi}_m, \quad (17)$$

$$\tilde{\Psi}_{1Z} = \tilde{\Psi}_{mZ}, \quad (18)$$

$$\frac{1}{b}\tilde{\Psi}_{mZZ} - \tilde{\Psi}_{1ZZ} = \frac{\chi}{\sqrt{\mathrm{Da}}}\tilde{\Psi}_{mZ}, \quad (19)$$

$$iK\bar{U}_{1Z}\tilde{\Psi}_1 + [-3K^2 + iK(C - \bar{U}_1)]\tilde{\Psi}_{1Z} + \tilde{\Psi}_{1ZZZ} = \frac{1}{b}\left[-3K^2 - \frac{b}{\mathrm{Da}} + iKC\right]\tilde{\Psi}_{mZ} + \frac{1}{b}\tilde{\Psi}_{mZZZ}. \quad (20)$$

At the liquid-liquid interface ($Z = 1$),

$$\tilde{\Psi}_1 = \tilde{\Psi}_2, \quad \tilde{H} = \tilde{\Psi}_1/(C - \bar{U}_1), \quad (21)$$

$$(\tilde{\Psi}_{1Z} - \tilde{\Psi}_{2Z}) + [\tilde{\Psi}_1/(C - \bar{U}_1)](\bar{U}_{1Z} - \bar{U}_{2Z}) = 0, \quad (22)$$

$$\tilde{\Psi}_{1ZZZ} - 3K^2\tilde{\Psi}_{1Z} - \mu_r\tilde{\Psi}_{2ZZZ} + 3\mu_r K^2\tilde{\Psi}_{2Z} + iK(C - \bar{U}_1)(\tilde{\Psi}_{1Z} - \rho_r\tilde{\Psi}_{2Z}) + iK(\bar{U}_{1Z}\tilde{\Psi}_1 - \rho_r\bar{U}_{2Z}\tilde{\Psi}_2) - \tilde{\Psi}_1/(C - \bar{U}_1)[(\bar{U}_{1Z} - \mu_r\bar{U}_{2Z})2K^2 + i\Gamma K^3] = 0, \quad (23)$$

$$[\tilde{\Psi}_{1ZZ} + K^2\tilde{\Psi}_1] + (\bar{U}_{1ZZ} - \mu_r\bar{U}_{2ZZ})\tilde{\Psi}_1/(C - \bar{U}_1) - \mu_r[\tilde{\Psi}_{2ZZ} + K^2\tilde{\Psi}_2] = 0. \quad (24)$$

V. NUMERICAL ANALYSIS

The coupled OS system in Eqs. (13)–(24) is an eigenvalue problem and is solved numerically to obtain the linear growth rate KC_i and the corresponding wave number K for the unstable modes. In this study, the most accurate D^2 algorithm proposed by Dongarra *et al.* [63] for the Chebyshev τ-QZ spectral method is employed to obtain the eigenvalues [64,65]. For this purpose, initially the computational domain is mapped onto $(-1,\ 1)$ by employing the transformations $Z_1 = -2Z + 1$, $Z_2 = \frac{2}{B-1}Z - \frac{B+1}{B-1}$, and $Z_m = \frac{2}{D_m}Z + 1$ for the lower, upper, and porous layer equations, respectively. Thereafter, introducing the variables $\eta(Z_1) = \tilde{\Psi}_1(Z)$, $\sigma(Z_2) = \tilde{\Psi}_2(Z)$, and $\zeta(Z_m) = \tilde{\Psi}_m(Z)$, the fourth-order ordinary differential equations (ODEs) (13)–(15) are transformed into the following six second-order ODEs in terms of the variables ξ, λ, and π:

$$L_1\eta \equiv \left(4d^2/dZ_1^2 - K^2\right)\eta = \xi, \tag{25}$$

$$L_1\xi - iK\bar{U}_1\xi + 2iKC_{11}\eta + iKC\xi = 0, \tag{26}$$

$$L_2\sigma \equiv \left\{[4/(B-1)^2]d^2/dZ_2^2 - K^2\right\}\sigma = \lambda, \tag{27}$$

$$\nu_r L_2\lambda - iK\bar{U}_2\lambda + 2iKC_{21}\sigma + iKC\lambda = 0 \tag{28}$$

$$L_m\zeta \equiv \left[(4/D^2)d^2/dZ_m^2 - K^2\right]\zeta = \pi, \tag{29}$$

$$L_m\pi - (b/\mathrm{Da})\pi + iKC\pi = 0. \tag{30}$$

The boundary conditions at the porous-solid and liquid-solid boundaries are derived in terms of the transformed variables as

$$\zeta_{Z_m}(-1) = \zeta(-1) = \sigma_{z_2}(1) = 0, \quad \sigma(1) = V. \tag{31}$$

The transformed boundary conditions at the porous-liquid interface are

$$\eta - \zeta = 0, \tag{32}$$

$$\eta_{Z_1} + \frac{1}{D}\zeta_{Z_m} = 0, \tag{33}$$

$$K^2\eta + \xi - \frac{K^2}{b}\zeta + \frac{2\chi}{D\sqrt{\mathrm{Da}}}\zeta_{Z_m} - \frac{1}{b}\pi = 0, \tag{34}$$

$$\begin{aligned} &iKC_{12}\eta + 2(2K^2 + iK\bar{U}_1)\eta_{Z_1} - 2\xi_{Z_1} \\ &+ \frac{2}{bD}\left[2K^2 + \frac{b}{\mathrm{Da}}\right]\zeta_{Z_m} - \frac{2}{bD}\pi_{Z_m} \\ &- C\left(2iK\eta_{Z_1} + \frac{2iK}{bD}\zeta_{Z_m}\right) = 0. \end{aligned} \tag{35}$$

The transformed boundary conditions at the liquid-liquid interface are

$$\eta - \sigma = 0, \tag{36}$$

$$C\left[2\eta_{Z_1} + (2/B-1)\,\sigma_{Z_2}\right] - [(2C_{11} + C_{12}) - (2C_{21} + C_{22})]\,\eta - 2\bar{U}_1\eta_{Z_1} - (2\bar{U}_1/B - 1)\sigma_{Z_2} = 0, \tag{37}$$

$$C(2K^2\eta + \xi - 2\mu_r K^2\sigma - \mu_r\lambda) + 2[(C_{11} - \mu_r C_{21}) - \bar{U}_1K^2]\eta - \bar{U}_1\xi + 2\mu_r\bar{U}_1K^2\sigma + \mu_r\bar{U}_1\lambda = 0, \tag{38}$$

$$\begin{aligned} &C^2\left[2iK\eta_{Z_1} + (2iK\rho_r/B - 1)\sigma_{Z_2}\right] + C\{-iK(2C_{11} + C_{12})\eta - 4(iK\bar{U}_1 + K^2)\eta_{Z_1} + 2\xi_{Z_1} + iK\rho_r(2C_{21} + C_{22})\sigma \\ &- (4/B-1)(\mu_r K^2 + iK\rho_r\bar{U}_1)\sigma_{Z_2} + [2\mu_r/(B-1)]\lambda_{Z_2}\} \\ &+ \left(\{2[(2C_{11} + C_{12}) - \mu_r(2C_{21} + C_{22})]K^2 + iK\bar{U}_1(2C_{11} + C_{12}) + i\Gamma K^3\}\eta - [2\mu_r\bar{U}_1/(B-1)]\lambda_{Z_2}\right. \\ &\left. + 2\left(2\bar{U}_1K^2 + iK\bar{U}_1^2\right)\eta_{Z_1} - 2\bar{U}_1\xi_{Z_1} - iK\bar{U}_1\rho_r(2C_{21} + C_{22})\sigma + [2/(B-1)]\left[2\mu_r\bar{U}_1K^2 + iK\rho_r\bar{U}_1^2\right]\sigma_{Z_2}\right) = 0. \end{aligned} \tag{39}$$

The subscripts Z_1, Z_2, and Z_m denote ordinary differentiation. The transformed ODEs are then expanded in terms of Chebyshev polynomials $T_n(z)$. For N Chebyshev polynomials, the eigenvalues are obtained for a $(6N + 12) \times (6N + 12)$ matrix corresponding to six second-order ODEs and twelve boundary conditions. The accuracy of the eigenvalues is tested by varying the number of polynomials and in the process the spurious eigenvalues are eliminated. The eigenvalues obtained from the Chebyshev τ-QZ spectral method are validated by solving the set of equations (25)–(39) employing the spectral collocation method [66]. The eigenvectors reported here are found using the spectral collocation method.

The numerical results are also validated against a number of configurations available in the literature. Figure 3(a) shows the variation in the linear growth coefficient KC_i vs wave number K plotted from the collocation method (circles) and Chebyshev τ-QZ method (solid line). The plots confirm that both numerical methods predict the same eigenvalues for the CFPM. Figure 3(b) reproduces a KC_i vs K plot for a two-layer CF [15] in the limit where the porous layer is almost impervious. Further, Fig. 3(c) shows a neutral stability diagram of a single layer of liquid confined between a rigid and a porous substrate [56]. This plot is obtained from the present analysis in the asymptotic limit where the upper plate velocity is zero and the liquid layers are kept identical. The code is also verified with the available results of the two-layer PPF in the limits where the porous layer is absent and the upper plate is stationary. Concisely, Fig. 3 corroborates the accuracy of the code at various asymptotic limits.

VI. RESULTS AND DISCUSSION

Previous theoretical studies [8] suggest that a two-layer PPF with equal density liquid layers is unstable either because of the long-wave interfacial mode when the condition $\mu_r > h_r^2$ is met or because of the finite-wave-number shear mode when

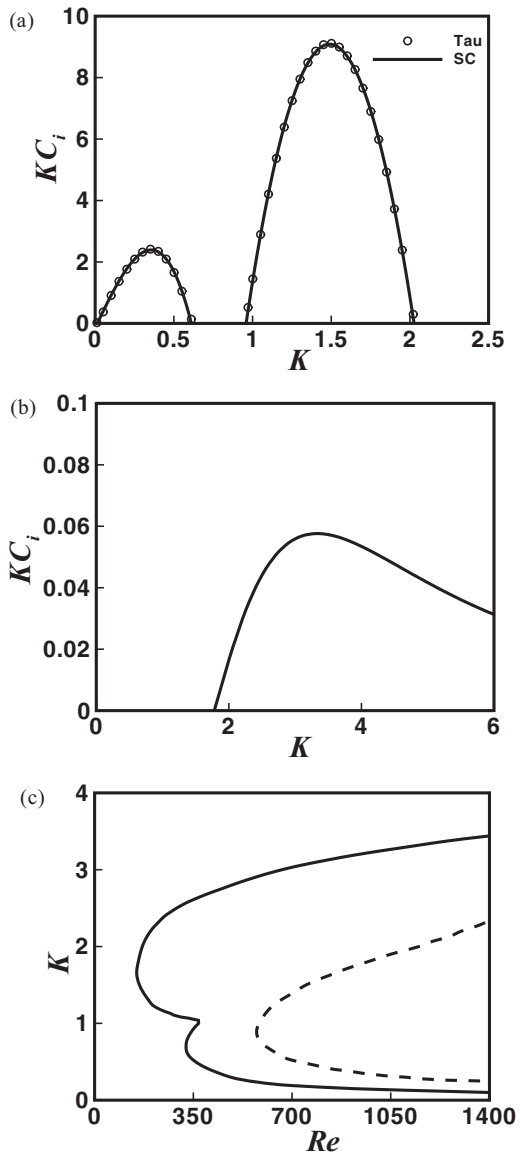

FIG. 3. (a) and (b) Variation of growth rate KC_i with wave number K for (a) $b = 0.5$, $D_m = 1$, $h_r = 1$, $\rho_r = 1$, $\mu_r = 5$, $\chi = 0.1$, $\Gamma = 16\,000$, and $\mathrm{Da} = 0.01$, with the solid line (dots) showing the result from the Chebyshev τ-QZ (collocation) method, and (b) $b = 0$, $D_m = 0.01$, $h_r = 6$, $\rho_r = 1$, $\mu_r = 2$, $\chi = 0$, $\Gamma = 0$, $\mathrm{Da} = 0.0001$, and $G = 0$. (c) Neutral stability diagram for the critical Reynolds number Re as a function of critical wave number K_c. The line solid (dashed) line corresponds to $h_r = 0.3$ (0.5). The other parameters are $b = 0.78$, $\rho_r = 0$, $\mu_r = 0$, $\chi = 0$, $\Gamma = 0$, $\mathrm{Da} = 0.0175$, and $G = 0$.

$\mu_r < h_r^2$ or is neutrally stable when $\mu_r = h_r^2$. The results discussed here highlight the importance of the underlying porous layer or the bounding moving plate of the CFPM largely around these conditions. It may be noted here that the results are reported in terms of upper to lower viscosity μ_r and thickness h_r ratios. To uncover the salient macro- and microscopic features of the CFPM, the following parameter space has been used for the analysis: $\rho_j \sim 1000$ kg/m^3, $\mu_j \sim 0.001-0.01$ Pa s, $d_j \sim 0.0001-0.1$ m, $\gamma \sim 0.02$ N/m, and x-directional velocity $\sim 10^{-4}$–0.5 m/s.

Figure 4 shows the presence of different instability modes under varied conditions. Figure 4(a) shows that when $\mu_r > h_r^2$, a CFPM on a porous layer with very small porosity and permeability shows only an interfacial mode of instability, as observed previously for the two-layer PPF between rigid and impervious surfaces [15,20]. With an increase in the velocity of the upper plate V, the frictional resistance progressively reduces the viscosity stratification across the interface, which in turn weakens the interfacial mode of instability. In contrast, the curves in Fig. 4(b) show that when the porosity b of the same configuration is increased, a finite-wave-number shear mode of instability appears beyond a critical porosity even when $\mu_r > h_r^2$. In this situation, an increase in porosity intensifies the flow inside the porous layer, which induces a larger slippage at the porous-liquid interface and reduces the frictional influence in the liquid layers to induce the shear mode of instability. Figure 4(c) shows that for a fixed b when V is progressively increased, the shear mode also can appear beyond a threshold plate velocity. A larger velocity of the bounding plate escalates the strength of the inertial force, which is the major reason for this shear mode at a larger V. Importantly, the shear modes reported in Figs. 4(b) and 4(c) are of different nature as compared to the conventional shear mode of two-layer CF or PPF under the condition $\mu_r < h_r^2$, which is shown separately in Fig. 4(d). The origin of these twin shear modes in the CFPM can be attributed to (i) the velocity of the moving plate at the top and (ii) the slippage at the porous-liquid interface due to the stronger flow inside the porous medium. The shear modes are found to coexist with the interfacial mode as dominant or subdominant modes even when the condition $\mu_r > h_r^2$ is met. Concisely, Fig. 4 confirms that movement of the bounding plate and the presence of a bounding porous layer can stimulate an additional shear mode of instabilities in a CFPM.

The neutral stability diagrams in Fig. 5 show more clearly the point of onset of the shear modes under the condition $\mu_r > h_r^2$. It may be noted here that the symbols i and s in the plots represent the interfacial and shear modes of instability, respectively. For ease of analysis, the shear mode appearing from the movement of the plate (from the porous layer) is denoted by $\mathrm{s^c}$ ($\mathrm{s^p}$) in the plots. In this figure, Re is changed by altering the plate velocity V. Curves with the notation i suggest the presence of a long-wave interfacial mode of instability under all conditions. In this plot, the progressive reduction in the span of unstable wave numbers with an increase in Re is due to a reduction in the viscosity stratification across the interface with an increase in V. Curve 1s shows that the finite-wave-number shear mode appears beyond a threshold Re and can coexist with the interfacial modes at larger V. Curves 2s–5s show that a reduction in porosity, thickness, and permeability and an increase in the stress-jump coefficient of the porous layer can delay the onset of the shear mode to a larger value of Re. The curves also suggest that the span of unstable wave numbers for the shear mode increases with a progressive increase in Re. Figure 5 shows that the shear modes associated with the movement of the upper plate or due to the presence of a porous medium appear only beyond a threshold Re but can grow stronger as the relative inertial influence increases with Re.

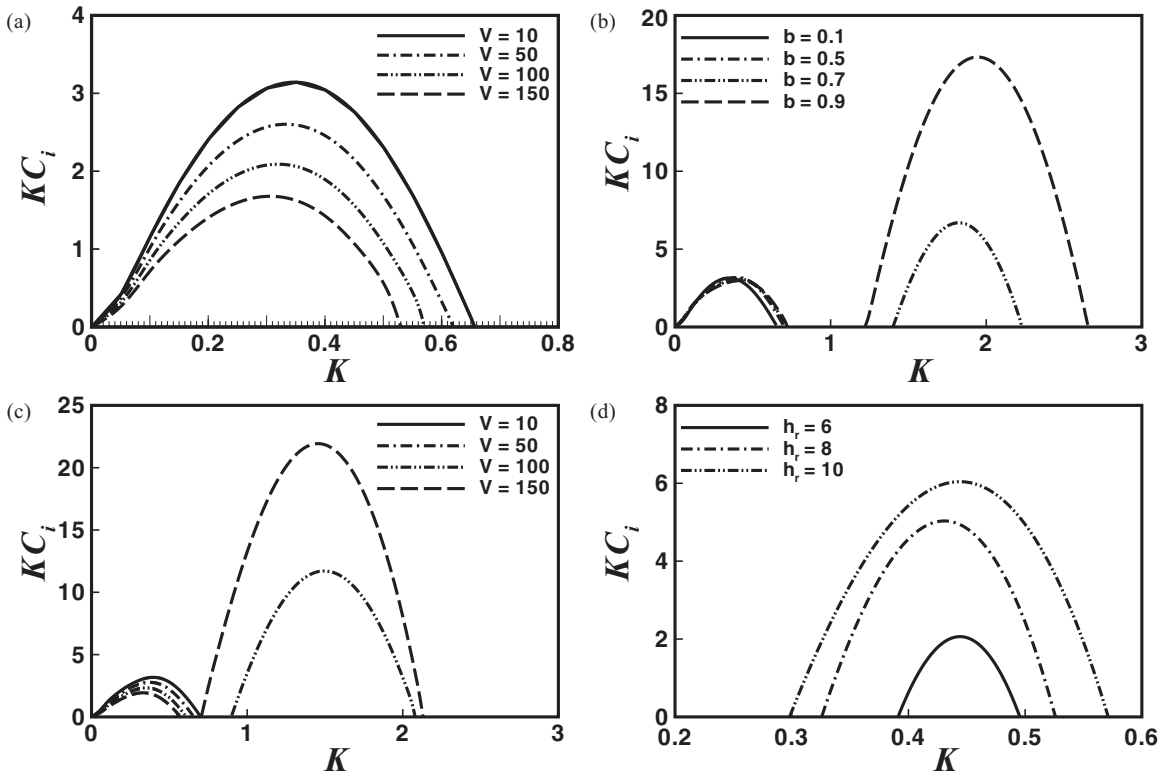

FIG. 4. Plots showing the variation of growth rate KC_i with wave number K for (a) $b = 0.1$, $D_m = 1$, $\rho_r = 1$, $\mu_r = 5$, $h_r = 1$, $\chi = 0.1$, and $\mathrm{Da} = 0.01$; (b) $V = 10$, $D_m = 1$, $\rho_r = 1$, $\mu_r = 5$, $h_r = 1$, $\chi = 0.1$, and $\mathrm{Da} = 0.01$; (c) $b = 0.5$, $D_m = 1$, $\rho_r = 1$, $\mu_r = 5$, $h_r = 1$, $\chi = 0.1$, and $\mathrm{Da} = 0.01$; and (d) $V = 50$, $b = 0.001$, $D_m = 10^{-3}$, $\rho_r = 1$, $\mu_r = 5$, $\chi = 0.0$, and $\mathrm{Da} = 10^{-6}$.

In Figs. 6 and 8–10, plot (a) shows the variation of KC_i with$K$ and plots (b)–(d) show the neutral stability plots of $(KC_i)_{\max}$ and $K_{\max}$, respectively, with the porous-media parameters. The dominant growth coefficient $(KC_i)_{\max}$ and wave number $K_{\max}$ are the global maxima from the KC_i vs K plots and the dominant wavelength is $\Lambda_{\max} = 2\pi/K_{\max}$. The

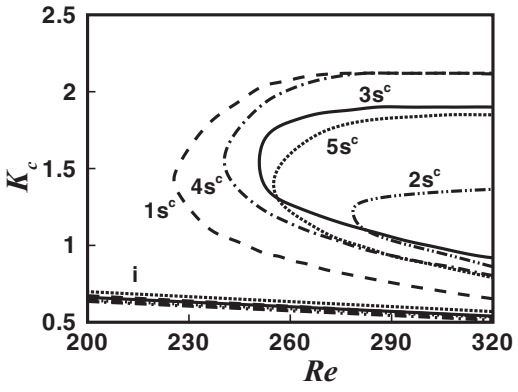

FIG. 5. Plot showing the neutral stability, which is the variation of K_c with Re when the plate velocity V is varied. The curves with i and s^c represent the interfacial and shear modes, respectively. Curves 1–5 represent $b = 0.5$, $b = 0.3$, $D_m = 0.7$, $\mathrm{Da} = 0.005$, and $\chi = 0.5$, respectively. The other parameters are kept fixed at $\mu_r = 5$, $\rho_r = 1$, $h_r = 1$, $b = 0.5$ (for curves 3–5); $D_m = 1$ (for curves 1, 2, 4, and 5); $\mathrm{Da} = 0.01$ (for curves 1–3 and 5), and $\chi = 0.1$ (for curves 1–4).

critical wave number K_c is obtained by enforcing the neutral stability condition $KC_i = 0$.

Figure 6 shows the influence of the porosity b of the porous layer on the inception and the growth of the different modes of the instabilities. Figure 6(a) shows that when $\mu_r > h_r^2$ and the porous layer is nearly impervious (small b), the CFPM can be unstable by only the long-wave interfacial mode (curve 1i). An increase in b allows a stronger flow inside the porous layer, which empowers the inertia force to subdue the viscous resistance at the lower layer. Consequently, a finite-wave-number shear mode of instability (curve 2s^c) appears alongside the interfacial mode (curve 2i). With an increase in b, the shear mode progressively becomes the dominant mode (curve 2s^c). Interestingly, at higher values of b, the presence of multiple shear modes (curves 3s^c and 3s^p) is observed. In such a situation, the shear mode that appeared at intermediate values of b becomes subdominant (curve 3s^c), whereas the newly appeared mode becomes the dominant mode (curve 3s^p) at very high values of b. Importantly, when b is kept constant and V is increased (curves 2s^c and 4s^c) the shear mode originating due to the movement of the plate becomes stronger. The neutral stability in Fig. 6(b) shows the conditions for the onset and coexistence of the different instability modes. Curves 1–3 in this plot represent different velocities; curve 2 was already discussed in Fig. 6(a). Curve 1 in Fig. 6(b) conveys that when $V = 10$, the interfacial mode is the only unstable mode at lower values of b. Beyond a critical value of $b_c = 0.614$, the frictional influence due to the flow inside the porous layer diminishes in such a manner that the

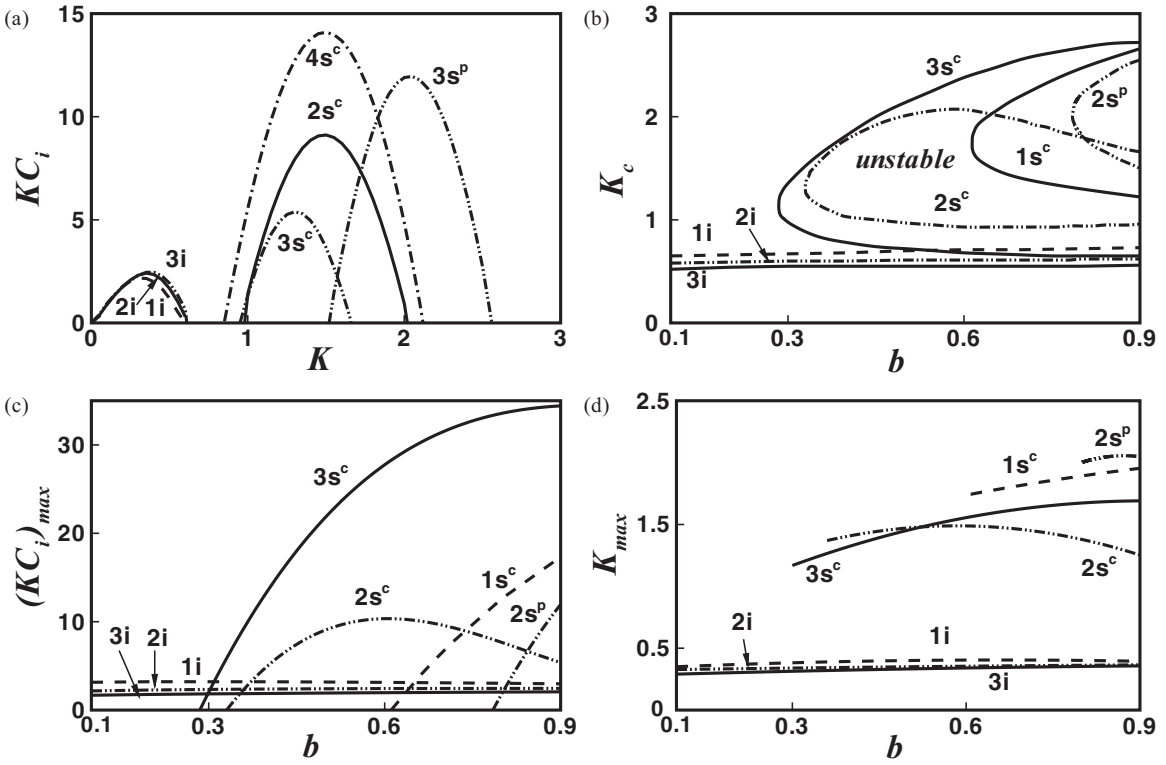

FIG. 6. Plots showing the influence of porosity b. The curves with i and s represent the interfacial and shear modes, respectively. (a) Variation of KC_i with K when $V = 90$ with curves 1–3 representing $b = 0.1$, 0.5, and 0.9, respectively. Curve 4 represents $V = 110$ and $b = 0.5$. (b)–(d) Variations of K_c, $(KC_i)_{\max}$, and $K_{\max}$ with b, respectively, with curves 1–3 representing $V = 10$, 90, and 150, respectively. The other parameters are $\mu_r = 5$, $\rho_r = 1$, $h_r = 1$, $\chi = 0.1$, $D_m = 1$, and $\mathrm{Da} = 0.01$.

finite-wave-number shear mode (curve $1s^c$) appears. With a further increase in b, as the flow empowers the inertial force, the span of unstable wave numbers increases for the shear mode, whereas the interfacial mode remains rather insensitive to the change in b. Curve 2 in this plot shows that if $V = 90$ and other conditions are kept the same, the shear mode appears at a much lower critical porosity $b_c = 0.33$. Interestingly, in such a situation, when b is progressively increased we observe the appearance of twin shear modes (curves $2s^c$ and $2s^p$), as discussed previously for Fig. 6(a). The plot also shows that with an increase in b at constant V, the span of unstable wave numbers reduces for the first mode (curve $2s^c$) before the second mode appears (curve $2s^p$). Further, the span of unstable wave numbers for the s^p mode is more towards the shorter-wavelength regime as compared to the s^c mode. Importantly, curve 3 in Fig. 6(b) shows that as V is increased to 150, the twin shear modes combine to show a single shear mode (curve $3s^c$). Figure 6(b) clearly show that an increase in the velocity of the upper plate can significantly reduce the viscous influence in a CFPM, which can expedite the onset of the shear mode of instability at a much lower value of b. Further, as observed in the base-state profiles in Fig. 2(b), an increase in b induces larger slippage at the porous-liquid interface, which is reflected in the increase in the span of unstable wave numbers for the shear mode with an increase in b in Fig. 6(b). Curves 1–3 in Figs. 6(c) and 6(d) represent $V = 10$, 90, and 150, respectively. The plots show that with a progressive increase of b and V, as the inertia is empowered, shorter-wavelength shear modes become the dominant mode of instability. Interestingly, as the viscosity stratification across the interface remains unchanged, the interfacial mode (curves 1i–3i) is insensitive to these influences. The plots highlight that at lower V only the s^c shear mode exists, at intermediate V the coexistence of both s^c and s^p shear modes is observed, and at higher V both the shear modes combine to form again a single s^c shear mode of instability. Interestingly, both shear modes are found to gain strength with V and b, whereas when twin modes are present the s^p (s^c) mode gains (loses) strength with an increase in b. Figure 6(d) shows that with an increase in b, the wavelength of the dominant shear mode progressively move towards the smaller-wavelength regime, whereas the same for the interfacial mode remains constant. It may be recalled here that the CFPM considered in Fig. 6 meets the criteria $\mu_r > h_r^2$ and $\rho_r = 1$ for which a two-layer PPF is unstable only through the interfacial mode of instability. The figure suggests that the introduction of the underlying porous layer together with movement of the upper plate can reduce the frictional influence and increase the relative strength of the inertia force to develop multiple finite-wave-number shear modes of instability. From the application point of view, the presence of these instability modes can be particularly useful in improving the heat and mass transfer and mixing characteristics especially in the microfluidic devices.

The origin of the twin shear modes is also investigated through an eigenfunction analysis. Figure 7 shows the magnitudes of the perturbed stream function $|\tilde{\Psi}_j|$ corresponding to

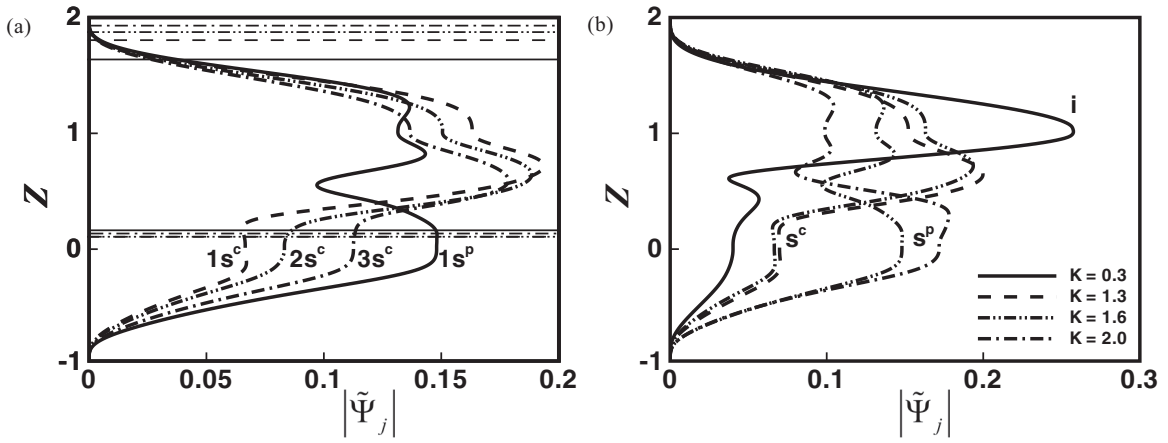

FIG. 7. (a) Eigenvectors at different porosities for $K = 1.6$. Curves $1s^p$ and $1s^c$ represent the twin shear modes at $b = 0.9$. Curve $2s^c$ represents the single shear mode at $b = 0.6$. The curve $3s^c$ represent the combined shear mode at $b = 0.9$ and $V = 150$. (b) Eigenvector at different K. The curves i, s^p, and s^c represent the interface mode and shear modes originating from the porous layer and Couette flow, respectively. The other parameters are $\mu_r = 5$, $b = 0.9$, $\rho_r = 1$, $h_r = 1$, $\chi = 0.1$, $D_m = 1$, and $\mathrm{Da} = 0.01$.

the eigenvalues obtained for the different modes in Fig. 6(a). In Fig. 7(a) the horizontal dashed, dash–double-dotted, dash-dotted, and solid lines show the locations for the critical layers ($U = C_r$), which are found to be situated in either the upper ($Z > 1$) or the lower layer ($0 < Z < 1$). Interestingly, all three (dashed) curves show three distinct changes in the slope for $|\tilde{\Psi}_j|$: (i) near the porous-liquid interface, (ii) near the liquid-liquid interface, and (iii) at the bulk of the lower layer. However, among these three slope changes in $|\tilde{\Psi}_j|$ one is found to be predominant. For the case with higher porosity ($b = 0.9$) two different eigenfunctions corresponding to the two different eigenvalues for the shear modes are analyzed at $V = 90$. The solid line $1s^p$ shows the largest variation in $|\tilde{\Psi}_j|$ near the porous-liquid interface ($Z = 0$), whereas the dashed curve $1s^c$ shows the same at the lower liquid layer. The dash–double-dotted curve $2s^c$ shows that a reduction in the porosity ($b = 0.6$) leads to an eigenfunction similar to curve $1s^c$. In this case we obtained only one eigenvalue for the shear mode. Further, the dash-dotted curve $3s^c$ shows an eigenfunction corresponding to the single eigenvalue obtained at $b = 0.9$ and $V = 150$, which again depicts the largest variation in $|\tilde{\Psi}_j|$ at the lower liquid layer. A comparison between curves $2s^c$ and $1s^p$ confirms that the change in $|\tilde{\Psi}_j|$ near the porous-liquid interface gains strength when the porosity is increased. In contrast, the same happens to $|\tilde{\Psi}_j|$ at the lower layer when the upper plate moves faster (curves $1s^c$, $2s^c$, and $3s^c$).

In Fig. 7(b) the eigenfunctions obtained at different values of K are shown. The plot corresponds to curve 3 in Fig. 6(a) ($b = 0.9$), which showed the existence of the interfacial mode at lower K, the appearance (disappearance) of a Couette shear mode (interfacial mode) at moderately higher K, the coexistence of both shear modes at higher values of K, and the existence of only the porous-medium mode at higher K. Following this trend, Fig. 7(b) shows the largest variation in $|\tilde{\Psi}_j|$ at the liquid-liquid interface (curve i) at lower values of $K(=0.3)$, which corresponds to the interfacial mode of instability. At moderately higher values of K $(=1.3)$, $|\tilde{\Psi}_j|$ shows a sharp variation in the lower layer (dashed line) when there exists only the Couette flow shear mode of instability. At $K = 1.6$, the coexistence of both Couette and porous-medium modes is observed, as shown by the dash–double-dotted lines with the marker s^c and s^p. In this case, the change of slope of $|\tilde{\Psi}_j|$ for the s^p mode takes place near the porous-liquid interface, whereas the same for the s^c mode occurs at the lower liquid layer. At higher values of K $(=2.0)$, we observe only the presence of the porous-medium mode as shown by the dash-dotted line with the marker s^p. Clearly, the eigenfunction plots shown in Fig. 7 connect the origin of the s^c and s^p modes with the movement of the plate at the top and the slippage at the porous-liquid interface, respectively.

Apart from the porosity of the porous layer, the thickness of the porous layer D_m can be an alternative parameter to reduce the frictional influence in a CFPM, as evident in Fig. 8. Figure 8(a) shows that when $\mu_r > h_r^2$ and D_m is very small, the CFPM can be unstable only through the interfacial mode (curve 1i). An increase in D_m allows flow inside the porous layer, which expedites the slippage at the porous-liquid interface developing a pair of finite-wave-number shear modes (curves $2s^c$ and $2s^p$) alongside the interfacial mode. The s^p mode of instability becomes the dominant mode at moderately high values of D_m. With a further increase in D_m, the s^p mode grows in strength, whereas the growth of the interfacial and s^c modes remains invariant. The neutral stability curve 1 in Fig. 8(b) conveys that when $V = 10$, interfacial mode (curve 1i) is the only unstable mode at lower values of D_m and the s^c mode (curve $1s^c$) appears only beyond a critical thickness ($D_m = 0.56$). With an increase in D_m, initially the span of unstable wave numbers increases for the shear modes and then becomes constant, whereas the same for the interfacial mode it always remains constant. Curve 2 in Fig. 8(b) shows that if V is increased to 90, the s^c mode appears at a similar critical thickness of the porous layer ($D_m = 0.56$). However, an s^p shear mode is also observed at a higher thickness of the porous layer ($D_m = 0.68$). Interestingly, curve 3 shows that at $V = 150$, the twin shear modes combine to show a single shear mode with a larger span of unstable wave numbers (curve $3s^c$). Previously, the base-state velocity profiles in Fig. 2(c)

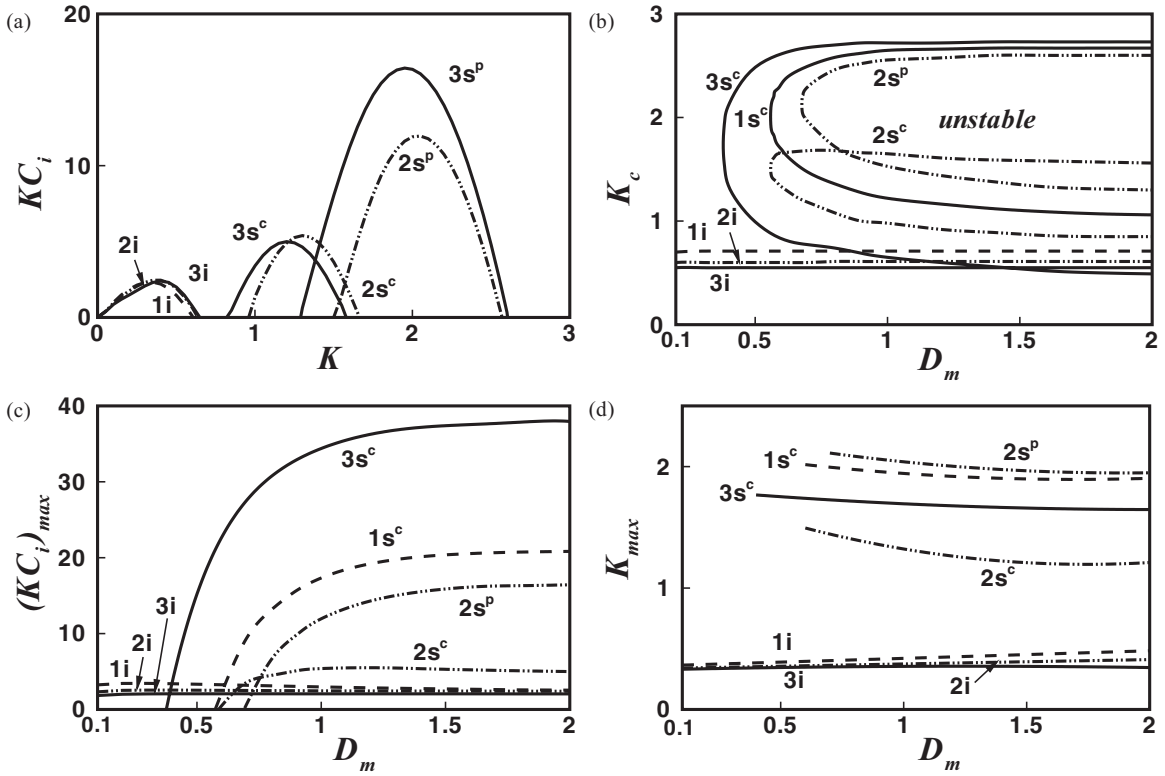

FIG. 8. Plots showing the influence of porous-medium thickness D_m. The curves with i and s represent the interfacial and shear modes, respectively. (a) Variation of KC_i with K when $V = 90$. Curves 1–3 represent $D_m = 0.1$, 1, and 2, respectively. (b)–(d) Variations of K_c, $(KC_i)_{\max}$, and $K_{\max}$ with D_m, respectively. Curves 1–3 represent $V = 10$, 90, and 150, respectively. The other parameters are $\mu_r = 5$, $\rho_r = 1$, $h_r = 1$, $b = 0.9$, $\chi = 0.1$, and $\mathrm{Da} = 0.01$.

showed that an increase in D_m induces larger slippage at the porous-liquid interface, which increases the convective influence in the CFPM. However, beyond a threshold D_m the reduction in the frictional influence saturates to a constant value, which is reflected in curves 1–3 of Figs. 8(c) and 8(d). The plots highlight that at very low D_m the interfacial mode is dominant and the shear mode appears only after a threshold porous layer thickness. With a progressive increase in D_m the shear mode becomes the dominant mode as the frictional influence reduces. However, beyond a threshold D_m, as the relative increase in the inertial influence saturates, $(KC_i)_{\max}$ reaches a constant value. The behavior of the CFPM here resembles a single-layer plane Poiseuille flow over a porous medium [55–57]. Briefly, Fig. 8 suggests that although the inertial influence due to the increase in the porous layer thickness can induce shear modes, the strength of these modes can only be increased until a threshold value of D_m.

Figure 9 shows that the permeability of the porous layer (Da) is another parameter that can influence the onset of shear modes. Curve 1i in Fig. 9(a) shows that in the presence of an impermeable porous layer only the interfacial mode is present. With a progressive increase in Da, as more flow is allowed inside the porous layer we observe the appearance of twin s^c and s^p shear modes of the instabilities. However, beyond threshold permeability, higher flow inside the porous layer weakens the flow in the fluid layers and the strength of the shear mode is found to decay. A CFPM on a highly permeable porous layer is unstable only through the interfacial mode, as shown by curve 3i. The neutral stability diagram in Fig. 9(b) confirms the appearance of the shear mode after a lower-threshold value of Da and the disappearance of the same beyond an upper-threshold value of Da. The plots also support that at lower V, only the s^c shear mode is observed, whereas at intermediate V, both shear modes coexist (curves $2s^c$ and $2s^p$). At higher V, the shear mode combines to show the presence of a single shear mode for a larger span of Da, as shown by curve $3s^c$. Curves 1–3 in Fig. 9(c) more clearly show that at low Da the interfacial mode is the dominant mode (curves 1i–3i). With a progressive increase in Da, the s^c (s^p) shear mode is the dominant mode at lower (higher) V. However, at very high velocities both shear modes combine to form a single shear mode, as depicted by curve $3s^c$. The strength of the shear modes decays beyond a limiting value of Da as the interfacial mode again becomes the dominant mode of instability. Figure 9(d) shows that with an increase in Da, the shear (interfacial) mode progressively move towards the larger- (smaller-) wavelength regime. Figure 9 shows that the twin shear modes can be observed only for a window of Da, while the interfacial mode of instability is the dominant mode for very high or very low Da.

Figure 10 summarizes the influence of the stress-jump coefficient χ on the different modes of instabilities. Curves 1i–3i in Fig. 10(a) show that an increase in χ infuses strength to the interfacial mode of instability. In contrast, the shear modes are only observed at some intermediate values of χ. Further, the shear modes disappear at higher values of χ. The plots clearly suggest that an increase in the stress-jump

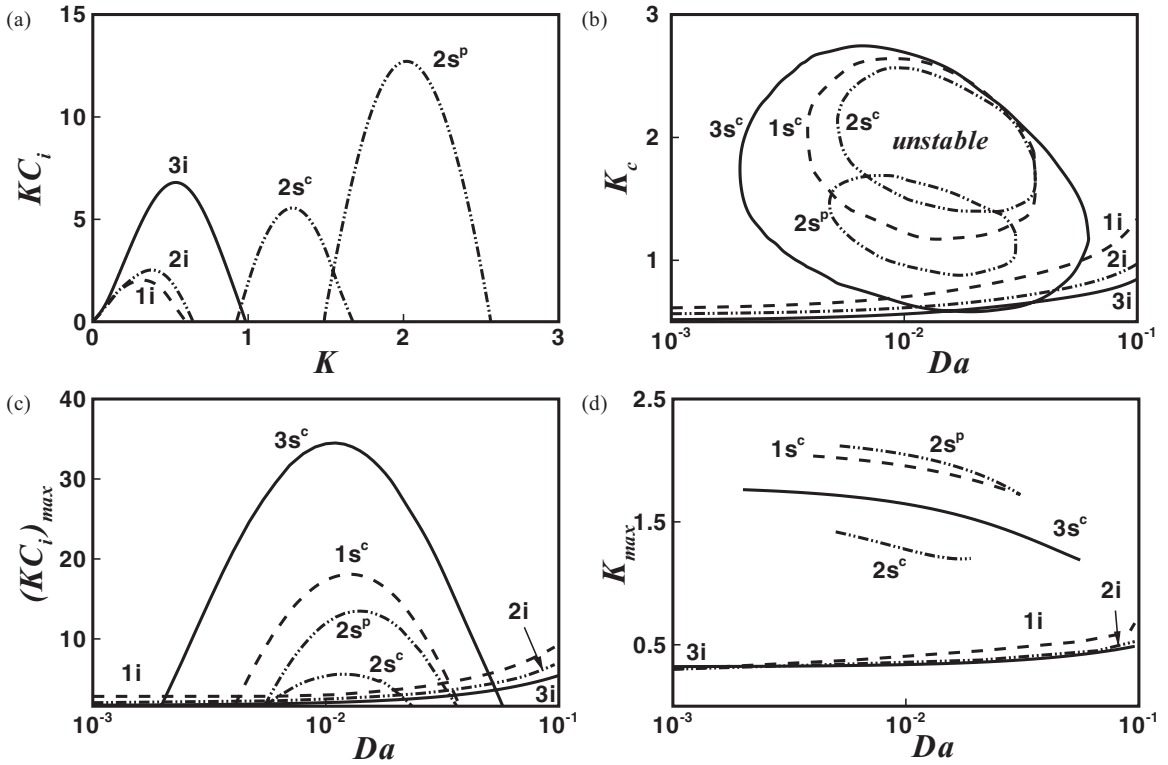

FIG. 9. Plots showing the influence of the Darcy number Da. Curves with i and s represent the interfacial and shear modes, respectively. (a) Variation of KC_i with K when $V = 90$. Curves 1–3 represent Da = 0.001, 0.01, and 0.096, respectively. (b)–(d) Variations of K_c, $(KC_i)_{\max}$, and $K_{\max}$ with Da, respectively. Curves 1–3 represent $V = 10$, 90, and 150, respectively. The other parameters are $\mu_r = 5$, $\rho_r = 1$, $h_r = 1$, $b = 0.9$, $\chi = 0.1$, $D_m = 1$, and Da = 0.01.

coefficient increases the frictional influence in the lower layer, which in turn increases the viscosity stratification between the liquid layers. In consequence, the shear modes become weaker as the frictional force dominates the inertial influence. The neutral stability diagram in Fig. 10(b) shows more clearly the weakening of the shear modes and insurgence of the interfacial mode with an increase in χ. Curves 1–3 in these plots confirm that the span of unstable wave numbers for the shear mode progressively reduces and the same for the interfacial mode gradually increases with an increase in χ. The plot also confirms that at lower V, only the s^c shear mode is observed, whereas at intermediate V, both shear modes coexist (curves $2s^c$ and $2s^p$). At higher V, the shear mode combines to show the presence of a single shear mode with a larger span of unstable wave numbers, as shown by curve $3s^c$. Curves 1–3 in Fig. 10(c) clearly highlight that at low χ the lesser frictional influence ensures a dominant shear mode of instability for a CFPM with a highly porous layer. However, with an increase in χ the interfacial mode becomes the dominant mode because of the increase in the frictional influence. The plot also suggests that the transition from a dominant shear to a dominant interfacial mode takes place at higher values of χ when V is larger. Figure 10(d) shows that with an increase in χ, the shear (interfacial) mode progressively move towards the larger- (smaller-) wavelength regime. Figures 11(a)–11(d) show phase diagrams for V vs the porous-medium parameters b, D_m, Da, and χ. In this figure we have identified the dominant mode among the interfacial and two shear modes of instabilities under varied conditions. The darker gray zones in the plots clearly depict that the s^c mode is the dominant one when the velocity of the top plate is high. Further, the s^p mode is found to be the dominant mode when the porous layers are of high porosity or are thick [Figs. 11(a) and 11(b)]. Figure 11(c) shows that at moderately high Da the s^p mode is the dominant mode, but at high Da the shear mode diminishes to make the interfacial mode as the dominant mode of instability, as observed previously in Fig. 9. Figure 11(d) shows that although the s^p mode is the dominant mode at lower values of χ, at the higher values where the frictional influence increases, the interfacial mode becomes the dominant mode. Figure 11 provides an overall idea of the dominance of the different unstable modes for a wide range of parameters.

VII. CONCLUSION

Instabilities of a pressure-driven two-layer plane Couette flow on a Darcy-Brinkman porous layer have been explored. An Orr-Sommerfeld analysis has been carried out by linearizing the governing equations and the boundary conditions. The OS system is solved numerically by employing two different methods to obtain the accurate eigenvalues, which are also validated against the results of the asymptotic cases that are available in the literature. The following are the important conclusions.

The study uncovers that apart from the conventional long-wave interfacial mode and finite-wave-number shear mode of instabilities of a two-layer CF, the CFPM may develop at least two additional finite-wave-number shear modes because of

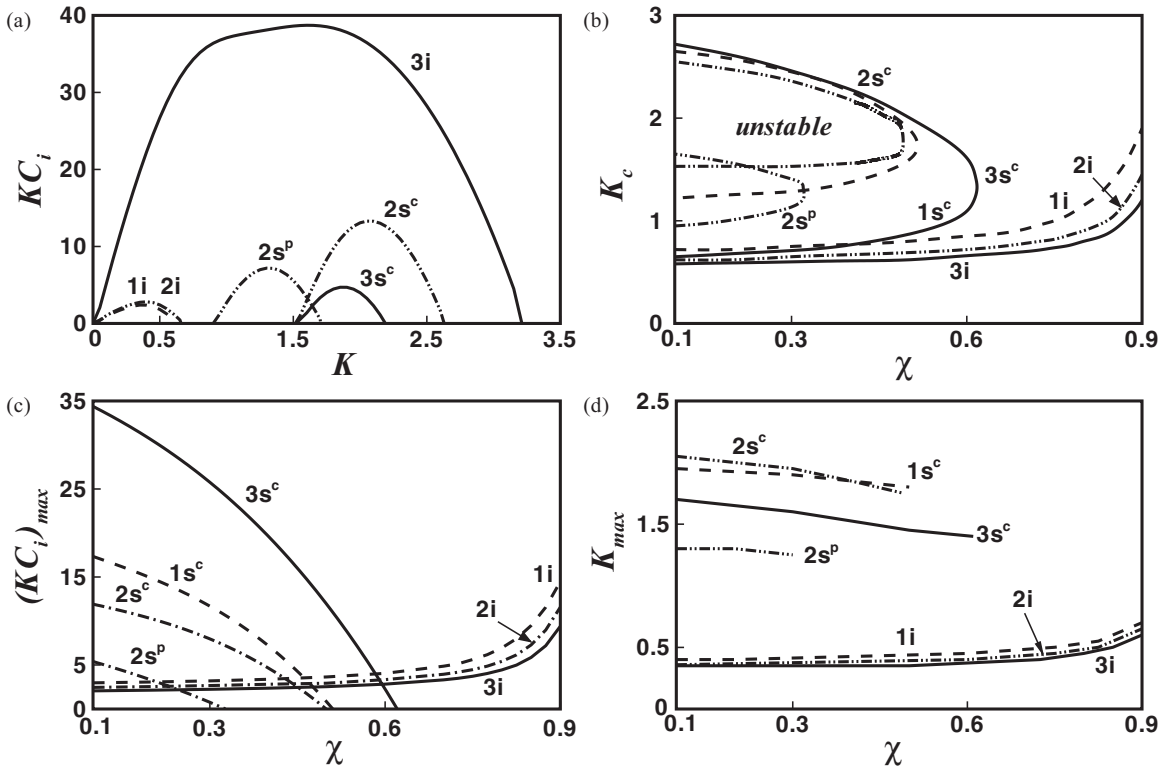

FIG. 10. Plots showing the influence of stress-jump coefficient χ. The curves with i and s represent the interfacial and shear modes, respectively. (a) Variation of KC_i with K when $V = 90$. Curves 1–3 represent $\chi = 0.0$, 0.5, and 1, respectively. (b)–(d) Variations of K_c, $(KC_i)_{\max}$, and $K_{\max}$ with χ, respectively. Curves 1–3 represent $V = 10$, 90, and 150, respectively. The other parameters are $\mu_r = 5$, $\rho_r = 1$, $h_r = 1$, $b = 0.9$, $\chi = 0.1$, $D_m = 1$, and $\mathrm{Da} = 0.01$.

the movement of the bounding plate and the flow inside the porous layer. Thus, for a CFPM, beyond a critical velocity of the moving plate or beyond some threshold values of the physical properties of the porous layer, a finite-wave-number shear mode (or modes) can be observed for almost all possible combinations of viscosity μ_r and thickness ratios of the liquid layers h_r. Conditionally, we also observe the presence of twin shear modes, one of which grows with bounding plate velocity, whereas the other grows with the increased slippage at the porous-liquid interface.

A permeable thick porous layer with high porosity is found to reduce frictional influence in the liquid layers especially when the lower layer is of low viscosity. The study shows that the influence of the porous layer affects the shear mode than the interfacial mode. The shear mode is more unstable at high porosity, whereas a porous layer with constant porosity and permeability can only increase the strength of the shear mode until a threshold thickness. The strength of the shear mode is found to increase and then decrease with the increase in permeability. The increased frictional influence with the increase in the stress-jump coefficient causes the reduction in strength of the shear modes and increase in strength of the interfacial modes. The analysis confirms that a transition from a dominant interfacial to a dominant shear mode can be performed only by tuning the velocity of the moving plate and the porous layer parameters for all possible μ_r and h_r.

Concisely, the study shows that the CFPM can be more unstable than conventional pressure-driven two-layer CF or PPF due to the flow inside the underlying porous layer coupled with the movement of the bounding plate. The augmented inertia (reduced friction) due to the presence of the porous layer or due to the movement of the bounding plate can more readily develop the shear modes of instabilities, which can eventually lead to a larger mixing, heat and mass transfer, and emulsification of the immiscible phases. The reported parameter bounds for the various unstable modes of the porosity, permeability, and thickness of the porous layer can be of importance in future studies related to the two-layer channel flow inside microfluidic devices.

ACKNOWLEDGMENTS

The initiation grant from IIT Guwahati and support from the DST through its fast track scheme SR/FTP/ETA-091/2009 are gratefully acknowledged. Discussions with Professor R. Usha during the derivations are gratefully acknowledged.

APPENDIX

The base-state governing equations are

$$\bar{U}_{1ZZ} = P_{0X} - G \sin\alpha, \tag{A1}$$

$$\bar{U}_{2ZZ} = (1/\mu_r)P_{0X} - (1/\nu_r)G \sin\alpha, \tag{A2}$$

$$(1/b)\bar{U}_{mZZ} - (1/\mathrm{Da})\bar{U}_m = P_{0X} - G \sin\alpha. \tag{A3}$$

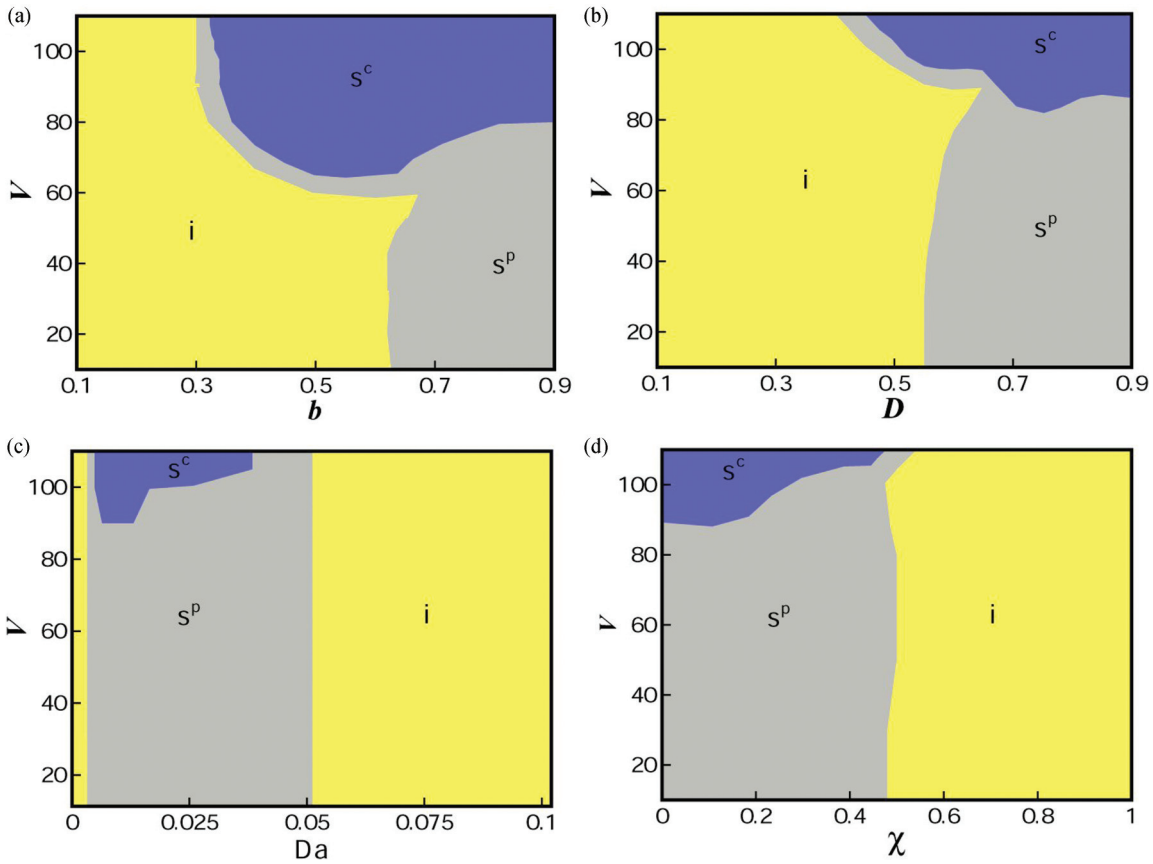

FIG. 11. (Color online) Contour plots showing the conditions for dominant interfacial i and shear s^p and s^c modes of the instabilities in the phase planes having V and porous-medium parameters for different (a) b, (b) D_m, (c) Da, and (d) χ. The other parameters are $\mu_r = 5$, $\rho_r = 1$, $h_r = 1$, $b = 0.9$, $\chi = 0.1$, $D_m = 1$, and $\mathrm{Da} = 0.01$.

The dimensionless no-slip boundary condition at the porous-solid interface ($Z = -D_m$) is

$$\bar{U}_m = 0. \tag{A4}$$

The dimensionless no-slip boundary condition at the liquid-solid interface ($Z = B$) is

$$\bar{U}_2 = V. \tag{A5}$$

The dimensionless form of the continuity of velocity and the stress-jump condition at the liquid-porous interface ($Z = 0$) are

$$\bar{U}_1 = \bar{U}_m, \tag{A6}$$

$$(1/b)\bar{U}_{mZ} - \bar{U}_{1Z} - (\chi/\sqrt{\mathrm{Da}})\bar{U}_m = 0. \tag{A7}$$

The dimensionless form of the continuity of velocity and the tangential stress balance at the liquid-liquid interface ($Z = 1$) are

$$\bar{U}_1 = \bar{U}_2, \tag{A8}$$

$$\bar{U}_{1Z} = \mu_r(\bar{U}_{2Z}). \tag{A9}$$

The above governing equations and boundary conditions yield

$$\bar{U}_1 = C_{11}Z^2 + C_{12}Z + C_{13}, \quad 0 \leqslant Z \leqslant 1, \tag{A10}$$

$$\bar{U}_2 = C_{21}Z^2 + C_{22}Z + C_{23}, \quad 1 \leqslant Z \leqslant B, \tag{A11}$$

$$\bar{U}_m = C_{m1}e^{MZ} + C_{m2}e^{-MZ} + C_{m3}, \quad -D_m \leqslant Z \leqslant 0, \tag{A12}$$

$$C_{11} = (P_{0X} - G^*)/2, \tag{A13}$$

$$C_{12} = \frac{a_2(P_{0X} - G^*) + C_{13}\phi}{a_1}, \tag{A14}$$

$$C_{13} = \left(\frac{a_4}{2a_3}\right)(P_{0X} - G^*) - \left(\frac{a_1 a_5}{2a_3}\right)(P_{0X} - \rho_r G^*), \tag{A15}$$

$$C_{21} = \frac{P_{0X} - \rho_r G^*}{2\mu_r}, \tag{A16}$$

$$C_{22} = \frac{a_2 + a_1}{a_1\mu_r}(P_{0X} - G^*) - \frac{1}{\mu_r}(P_{0X} - \rho_r G^*) + \frac{\phi}{a_1\mu_r}C_{13}, \tag{A17}$$

$$C_{23} = -\frac{(P_{0X} - \rho_r G^*)B^2}{2\mu_r} - C_{22}B, \tag{A18}$$

$$C_{m1} = -\left(\frac{\mathrm{Da}\,(F_- - 1)\,(P_{0X} - G^*) + C_{13}F_-}{a_1}\right), \tag{A19}$$

$$C_{m2} = \frac{\mathrm{Da}\,(F_+ - 1)\,(P_{0X} - G^*) + C_{13}F_+}{a_1}, \tag{A20}$$

$$C_{m3} = -\mathrm{Da}(\,P_{0X} - G^*), \tag{A21}$$

where $\phi = F_- J_+ + F_+ J_-$, $\psi = \chi(F_+ - F_-)\mathrm{Da}^{-1/2} - 2(b\,\mathrm{Da})^{-1/2}$, $G^* = G\sin\alpha$, $F_+ = e^{\sqrt{b/\mathrm{Da}}\,D_m}$, $M = \sqrt{b/\mathrm{Da}}$, $F_- = e^{-\sqrt{b/\mathrm{Da}}D_m}$, $J_+ = (\sqrt{1/b\,\mathrm{Da}} + \chi/\sqrt{\mathrm{Da}})$, $J_- = (\sqrt{1/b\,\mathrm{Da}} - \chi/\sqrt{\mathrm{Da}})$, $a_1 = (F_+ - F_-)$, $a_5 = (B-1)^2$, $a_2 = [\mathrm{Da}(\phi - J_- - J_+) + a_1\chi\sqrt{\mathrm{Da}}]$, $a_3 = (B-1)\phi + (\phi + a_1)\mu_r$, and $a_4 = (1 - B - \mu_r)2a_2 + (2 - 2B - \mu_r)a_1$.

[1] H. S. Yu and E. M. Sparrow, ASME J. Heat Transfer **91**, 51 (1969).
[2] H. H. Hu and D. D. Joseph, J. Fluid Mech. **205**, 359 (1989).
[3] C. D. Han, *Multiphase Flow in Polymer Processing* (Academic, New York, 1981).
[4] P. A. Davidson and R. I. Lindsay, J. Fluid Mech. **362**, 273 (1998).
[5] M. Ehrhardt, J. Fuhrmann, A. Linke, and E. Holzbecher, *Mathematical Modeling of Channel-Porous Layer Interfaces in PEM Fuel Cells*, in Proceedings of FDFC 2008—Fundamentals and Developments of Fuel Cells Conference 2008 (University of Nancy, Nancy, France, 2008).
[6] P. Jiang, M.-H. Fan, G.-S. Shi, and Z.-P. Ren, Int. J. Heat Mass Transfer **44**, 1039 (2001).
[7] M. B. Allen, G. A. Behie, and J. A. Trangenstein, *Multiphase Flow in Porous Media: Mechanics, Mathematics, and Numerics* (Springer, Berlin, 1988).
[8] A. R. A. Khaled and K. Vafai, Int. J. Heat Mass Transfer **46**, 4989 (2003).
[9] C. S. Yih, J. Fluid Mech. **27**, 337 (1967).
[10] C. E. Hickox, Phys. Fluids **14**, 251 (1971).
[11] A. P. Hooper and W. G. C. Boyd, J. Fluid Mech. **128**, 507 (1983).
[12] A. P. Hooper and R. Grimshaw, Phys. Fluids **28**, 37 (1985).
[13] A. P. Hooper, Phys. Fluids **28**, 1613 (1985).
[14] A. P. Hooper and W. G. C. Boyd, J. Fluid Mech. **179**, 201 (1987).
[15] A. P. Hooper, Phys. Fluids A **1**, 7 (1989).
[16] D. D. Joseph, M. Renardy, and Y. Renardy, J. Fluid Mech. **141**, 309 (1984).
[17] Y. Renardy, Phys. Fluids **28**, 3441 (1985).
[18] Y. Renardy, Phys. Fluids **30**, 1627 (1987).
[19] T. I. Hesla, F. R. Pranckh, and L. Preziosi, Phys. Fluids **29**, 2808 (1986).
[20] S. G. Yiantsios and B. G. Higgins, Phys. Fluids **31**, 3225 (1988).
[21] F. Charru and J. Fabre, Phys. Fluids **6**, 1223 (1994).
[22] P. Barthelet, F. Charru, and J. Fabre, J. Fluid Mech. **303**, 23 (1995).
[23] F. Charru and P. Barthelet, Physica D **125**, 311 (1999).
[24] F. Albart and F. Charru, Eur. J. Mech. B: Fluids **19**, 229 (2000).
[25] F. Charru and E. J. Hinch, J. Fluid Mech. **414**, 195 (2000).
[26] B. S. Tilley, S. H. Davis, and S. G. Bankoff, J. Fluid Mech. **277**, 55 (1994).
[27] B. S. Tilley, S. H. Davis, and S. G. Bankoff, Phys. Fluids **6**, 3906 (1994).
[28] M. E. Chales and L. U. Lilleleht, J. Fluid Mech. **22**, 217 (1965).
[29] T. W. Kao and C. Park, J. Fluid Mech. **52**, 401 (1972).
[30] P. G. Drazin and W. H. Reid, *Hydrodynamic Stability* (Cambridge University Press, London, 1981).
[31] D. D. Joseph and Y. Renardy, *Fundamentals of Two-Fluid Dynamics, Part I: Mathematical Theory and Applications* (Springer, Berlin, 1993).
[32] K. P. Chen, Appl. Mech. Rev. **48**, 763 (1995).
[33] P. A. M. Boomkamp and R. H. M. Miesen, Int. J. Multiphase Flow **22**, 67 (1996).
[34] J. Jang and S. S. Lee, Sens. Actuat. **80**, 84 (2000).
[35] H. H. Bau, J. Zhong, and M. Yi, Sens. Actuators B **79**, 207 (2001).
[36] S. Qian, J. Z. Zhu, and H. H. Bau, Phys. Fluids **14**, 3584 (2002).
[37] S. Qian, S. W. Joo, Y. Jiang, and M. A. Cheney, Mech. Res. Commun. **36**, 82 (2008).
[38] S. Qian and H. H. Bau, Mech. Res. Commun. **36**, 10 (2009).
[39] O. Ozen, N. Aubry, D. T. Papageorgiou, and P. G. Petropoulos, Phys. Rev. Lett. **96**, 144501 (2006).
[40] O. Ozen, N. Aubry, D. T. Papageorgiou, and P. G. Petropoulos, J. Fluid Mech. **583**, 347 (2007).
[41] D. Bandyopadhyay, P. D. S. Reddy, A. Sharma, S. W. Joo, and S. Qian, Theor. Comput. Fluid Dyn. **26**, 23 (2012).
[42] P. D. S. Reddy, D. Bandyopadhyay, S. W. Joo, A. Sharma, and S. Qian, Phys. Rev. E **83**, 036313 (2011).
[43] B. Ray, P. D. S. Reddy, D. Bandyopadhyay, S. W. Joo, A. Sharma, S. Qian, and G. Biswas, Electrophoresis **32**, 1 (2011).
[44] B. Ray, P. D. S. Reddy, D. Bandyopadhyay, S. W. Joo, A. Sharma, and S. Qian, Theor. Comput. Fluid Dyn. **26**, 311 (2011).
[45] B. Ray, D. Bandyopadhyay, A. Sharma, S. W. Joo, S. Qian, and G. Biswas, Microfluid. Nanofluid., doi:10.1007/s10404-012-1122-4.
[46] G. S. Beavers and D. D. Joseph, J. Fluid Mech. **30**, 197 (1967).
[47] J. P. Pascal, J. Phys. D **32**, 417 (1999).
[48] J. P. Pascal, J. Non-Newtonian Fluid Mech. **133**, 109 (2006).
[49] M. R. Sadiq and R. Usha, Phys. Fluids **20**, 022105 (2008).
[50] M. R. Sadiq, R. Usha, and S. W. Joo, Chem. Eng. Sci. **65**, 4443 (2010).
[51] J. A. Ochoa-Tapia and S. Whitaker, Int. J. Heat Mass Transf. **30**, 2635 (1995).
[52] U. Thiele, B. Goyeau, and M. G. Velarde, Phys. Fluids **21**, 014103 (2009).
[53] L. E. Payne and B. Straughan, J. Math. Pures Appl. **77**, 317 (1998).
[54] M. H. Chang, F. Chen, and B. Straughan, J. Fluid Mech. **564**, 287 (2006).
[55] L. Dong and D. Johnson, Int. J. Heat Fluid Flow **26**, 133 (2005).
[56] A. Hill and B. Straughan, J. Fluid Mech. **603**, 137 (2008).
[57] A. Hill and B. Straughan, Adv. Water Resour. **32**, 1609 (2009).
[58] A. Hill and B. Straughan, Proc. R. Soc. London Ser. A **465**, 207 (2009).
[59] B. Goyeau, D. Lhuillier, D. Gobin, and M. G. Velarde, Int. J. Heat Mass Transfer **46**, 4071 (2003).
[60] R. Liu, Q. S. Liu, and S. C. Zhao, Phys. Fluids. **20**, 104105 (2008).
[61] R. Liu and Q. S. Liu, Phys. Rev. E **80**, 036316 (2009).
[62] R. Liu and Q. S. Liu, Phys. Fluids **22**, 074101 (2010).
[63] J. J. Dongarra, B. Straughan, and D. W. Walker, Appl. Numer. Math. **22**, 399 (1996).
[64] S. A. Orszag, J. Fluid Mech. **50**, 689 (1971).
[65] D. Gottlieb and S. A. Orszag, *Numerical Analysis of Spectral Methods: Theory and Applications*, CBMS-NSF Regional Conference Series in Applied Mathematics Vol. 26 (SIAM, Philadelphia, 1977).
[66] J. A. C. Weideman and S. C. Reddy, ACM Trans. Math. Software **26**, 465 (2000).